Experimental identification of a bistable device for seismic energy dissipation

Mechanical Systems and Signal Processing 256 (2026) 114512

Contents lists available at ScienceDirect

Mechanical Systems and Signal Processing

journal homepage: www.elsevier.com/locate/ymssp

Full Length Article

Experimental identification of a bistable device for seismic energy dissipation

L. Scussolini [a,*], V. Cavanni [a], G. Miraglia [a,c], A. De Marchi [b], R. Ceravolo [a,c]

[a] Department of Structural, Geotechnical and Building Engineering, Politecnico di Torino 10129 Torino, Italy
[b] Former Faculty Professor, Politecnico di Torino 10129 Torino, Italy
[c] Responsible Risk Resilience Interdepartmental Centre (R3C), Politecnico di Torino 10129 Torino, Italy

ARTICLE INFO

Keywords:
Bistable metamaterials
Nonlinear time-varying systems
Instantaneous Bayesian characterisation
Seismic energy dissipation
Experimental identification

ABSTRACT

This work describes a novel method for experimentally measuring and identifying dynamic parameters of bistable systems. The investigated samples are physical models of unit cells of mechanical metamaterials used for seismic energy dissipation. In order to identify this type of nonlinear systems, the paper proposes a new instantaneous probabilistic algorithm, which is capable of extracting the causal components of the dynamic response from the random ones. This is especially relevant for nonlinear systems exhibiting abrupt transitions between dynamical regimes, whose frequency content can evolve significantly over time. In particular, the approximate Bayesian computation (ABC) approach is extended to the time-frequency representation of non-stationary dynamic responses typical of bistable systems. The method was tested on experimental measurements of 3D-printed bistable samples with the final goal of estimating the instantaneous energy dissipated under different external excitations, proving the device's effectiveness.

1. Introduction

Nonlinear system identification is a well-known challenging task, especially when dealing with experimental measurements. Indeed, finding a nonlinear model which could predict the behaviour of a system implies two main issues: first, the determination of the model structure which describes the input-output relationship is often not unique; second, the estimation of the parameters of the model structure is not trivial, and requires high computational effort [1]. If the nonlinear component of the response is negligible, the accuracy of the solution is not affected, and linear techniques can be relied upon. However, if the nonlinear effects are significant, as frequently happens under strong excitations, such as earthquakes, simplifying assumptions (Hooke's law, small displacements, etc.) no longer hold and one should refer to more sophisticated models and methods [2]. This is the case of bistable systems, i.e., systems characterised by three static equilibrium points, two of which are stable and one unstable.

While in the literature one can find various examples of modelling and parameter estimation for bistable systems, for the purposes of this discussion one can refer to [3–6]. Bistability can be achieved using mechanical metamaterials, i.e. engineered materials with properties that do not exist in nature [7], which prove particularly useful in the field of energy absorption/dissipation [8–11]. Thus, an appealing idea is to exploit these materials for seismic energy dissipation. However, as various geometries and materials can be used to achieve bistability, finding a technique that can correctly identify the nonlinear parameters governing the response is a fundamental

* Corresponding author.
E-mail address: linda.scussolini@polito.it (L. Scussolini).

https://doi.org/10.1016/j.ymssp.2026.114512
Received 4 February 2026; Received in revised form 30 April 2026; Accepted 26 May 2026
Available online 2 June 2026

aspect of the identification task, and, especially in experimental settings, uncertainties may arise from the definition of boundary conditions, materials, and manufacturing.

Several techniques have been proposed to solve the identification problem for nonlinear systems [12–14]. A first classification of identification techniques in the nonlinear field may be represented by the distinction into parametric and non-parametric approaches. In the first case, one should know a priori what the physical characteristics of the system are, in order to formulate the mathematical model: some examples can be found in [15–17]. The parametric identification problem has been frequently solved through estimation techniques based on the least square method [18] or optimisation algorithms [19]. On the other hand, non-parametric methods do not include hypotheses on the type and location of nonlinearities, and the estimated quantities are not directly related to physical properties of the system. A further subdivision may be done into instantaneous and non-instantaneous approaches. An instantaneous approach provides an estimate of the parameters for each instant of time. This is particularly useful in the field of structural health monitoring (SHM), where it is often necessary to look for a variation of parameters over time to detect damage or degradation. Instantaneous methods can be further divided into online, such as the extended Kalman filter (EKF) [20] and unscented Kalman filter (UKF) [21], and offline methods, which usually require passing through the analytic signal [22–24]. In general, time-series based methods have been extensively used for the analysis of experimental nonlinear systems, especially for the characterisation of system response under noisy conditions and for tracking stiffness-related variations under dynamic excitation [25,26].

Another strategy is based on the joint time-frequency representation of the response signals, with possible implementations both online and offline, depending on the type of transform used [27–29]. For instance, quadratic transforms, especially those belonging to the Cohen class, being non-causal (i.e., they hold the correlative structure of the Wigner distribution) do not allow an online implementation. Conversely, linear transforms, such as the short-time Fourier transform (STFT), use sliding windows to divide the signal into time-localised components, supporting an online implementation (except for the estimation lag introduced by the analysis window length) at relatively low computational cost. Some contributions, which provide useful insights for this research, have focused on the problem of high uncertainty in parameter estimation, typical of nonlinear systems [30], including Markov chain Monte Carlo simulations [31–33] and, more generally, Bayesian inference [34–36]. In the task of identification of nonlinear time-varying parameters, one may combine these techniques with other methods suitable for an instantaneous implementation, such as Kalman filtering techniques [37,38], reinforcement learning [39], and stochastic simulation-based approaches, e.g., particle filters [40].

It is worth noting that Bayesian approaches formulated in the time-domain may provide uncertainty quantification, e.g., see [41], but do not explicitly incorporate information on the spectral components. As a result, they are not naturally suitable to describe the evolution of spectral content in the non-stationary response of nonlinear and time-varying systems. Time-frequency methods may overcome this limitation by extending the concept of local stationarity to the case of nonlinear and time-varying systems, explicitly identifying when specific spectral components occur in time [42]. This is particularly relevant for nonlinear systems exhibiting abrupt transitions between dynamical regimes, whose frequency content may evolve over time. More importantly, in these systems the challenge linked to the difficulty in unraveling nonlinearity from non-stationarity may arise [43], making signals inherently difficult to analyse when viewed from separate time or frequency perspectives.

In this context, the need for a technique capable of capturing the instantaneous behaviour of highly nonlinear systems characterised by uncertainty in parameters, i.e. the bistable ones, is fundamental. This requirement is even more pressing when considering the possible use of these systems in seismic devices, namely the instantaneous dissipation and/or absorption, which is critical in real-world applications [44–46]. For the purposes of this work, approximate Bayesian computation (ABC) [47] is combined with a time-frequency estimator in order to obtain an instantaneous probabilistic evaluation of the nonlinear parameters governing the bistable response and, consequently, of the instantaneous dissipated energy. The ABC algorithm is convenient when the likelihood function is particularly challenging to compute, if not intractable. Moreover, ABC has already proved effective in the treatment of bistable, and eventually multistable, systems [48]. This formulation addresses the limited ability of existing approaches to provide instantaneous uncertainty estimates in markedly time-varying and nonlinear systems, particularly for parameters related to damping characteristics. Bistable systems represent a clear example in which time-varying properties and dissipative characteristics require associated uncertainty estimation in addition to mean prediction, with clear implications for engineering applications. This technique has been validated on experimental recordings obtained by testing a 3D-printed cosine-shaped beam (CSB) bistable sample.

The paper is organised as follows. Section 2 presents the bistable device, as well as the single degree-of-freedom (SDoF) model employed for the identification task, introducing the basic concepts associated with bistable dynamics. Section 3 outlines the procedure for the probabilistic instantaneous identification of nonlinear parameters to be used on the experimental signals. Section 4 describes the laboratory setup, including the prototype testing machine and the samples obtained through 3D printing. Section 5 reports the results of the nonlinear system identification conducted on the experimental signals. Section 6 contains a discussion on the performance of bistable devices in dissipating the energy transmitted by ground motion in terms of an equivalent damping ratio based on dissipation cycles. Conclusions are finally drawn in Section 7.

2. Energy dissipation in bistable systems and devices

The type of energy dissipation devices experimentally investigated and characterised in this work is designed to exploit bistable dynamics for passive seismic control. Nonlinear systems can in general exhibit one or more forms of response coexisting at the same excitation condition. In the case of bistable systems, two characteristic regimes of oscillations can be identified: (i) *intrawell* oscillations, around one of the two stable equilibrium points, and (ii) *interwell* oscillations, around the unstable equilibrium point. Consequently, the potential energy of bistable systems is referred to as double-well potential, whose shape dictates both the threshold for the activation of snap-through and the elevated velocities linked to interwell oscillations. Conceptually, the device can be described as a

nonlinear extension of the tuned mass damper (TMD) [49,50], but, differently from classical TMDs, it does not operate as a traditional absorber, since its dissipation capabilities remain elevated also in case of small viscous coefficient. This is due to the high velocities that the bistable system exhibits during the transition between the stable and unstable equilibrium points [51,52].

Bistable dynamics can be obtained by exploiting the unit cells of negative stiffness mechanical metamaterials, whose nonlinear properties are determined by specific geometries rather than the constitutive material. In this research, a CSB geometry was selected given its greater energy trapping capacity compared to similar tilted configurations [53]. A 3D representation of the device is reported in Fig. 1. The device architecture has two main features: a mass attachment; and a nonlinear mechanism built into the CSB unit cell. The interaction between these two components ensures that seismic energy is efficiently transferred and dissipated through successive snap-through events. From the point of view of the system dynamics, it is clear that the critical variable for the performance of the device is the value of the velocity that occurs during the transition across the unstable position, which is responsible for the energy dissipation.

The stiffness restoring force of the bistable device can be approximated by a polynomial nonlinearity [54]. Also neglecting the mass of the CSB with respect to the vibrating mass, the equation of motion of the generic polynomial oscillator of mass m and viscous damping c reads:

$$\begin{cases} m\ddot{y} + f_{r,d}(\dot{y}) + f_{r,s}(y) = u(t) \\ f_{r,d} = c\dot{y} \\ f_{r,s} = \sum_{l=0}^{L} k_l y^l \end{cases} \tag{1}$$

where y, $\dot{y}$, and $\ddot{y}$ are the displacement, velocity, and acceleration of the system and $u(t)$ is the generic external excitation. The stiffness restoring force, $f_{r,s}$, is the rate-independent component of the response, described by the system stiffness coefficients k_l, and the maximum polynomial order L. Conversely, $f_{r,d}$ is the rate-dependent contribution, in the form of linear viscous damping. If the stiffness restoring force $f_{r,s}$ is an odd function of y, i.e., it shows a symmetric potential, then all the even coefficients vanish. The governing equation of motion for the majority of bistable systems is a direct consequence of Eq. (1) truncated up to the third order. In particular, to obtain bistability the *linear* stiffness should be necessarily defined as $k_1 < 0$. Hence, Eq. (1) can be rewritten as:

$$m\ddot{y} + c\dot{y} + k_1 y + k_3 y^3 = u(t) \tag{2}$$

with $k_3 > 0$ as the *cubic* stiffness. The unforced static solution leads to the determination of the equilibrium configurations of the bistable system, by solving the equation expressed by:

$$k_1 y + k_3 y^3 = 0 \tag{3}$$

The solutions to the polynomial equation are $y = \pm\sqrt{-k_1/k_3}$, and $y = 0$. These are the stable and the unstable equilibrium points, respectively. Although Eq. (2) may appear the same as the governing equation of a classical Duffing oscillator, the static equilibrium, with a unique solution given by $y = 0$, reveals that the latter is inherently monostable. Consistently, the truncation to a third-order polynomial in the stiffness restoring force $f_{r,s}$ is justified under the assumption of finite but sufficiently small displacements around

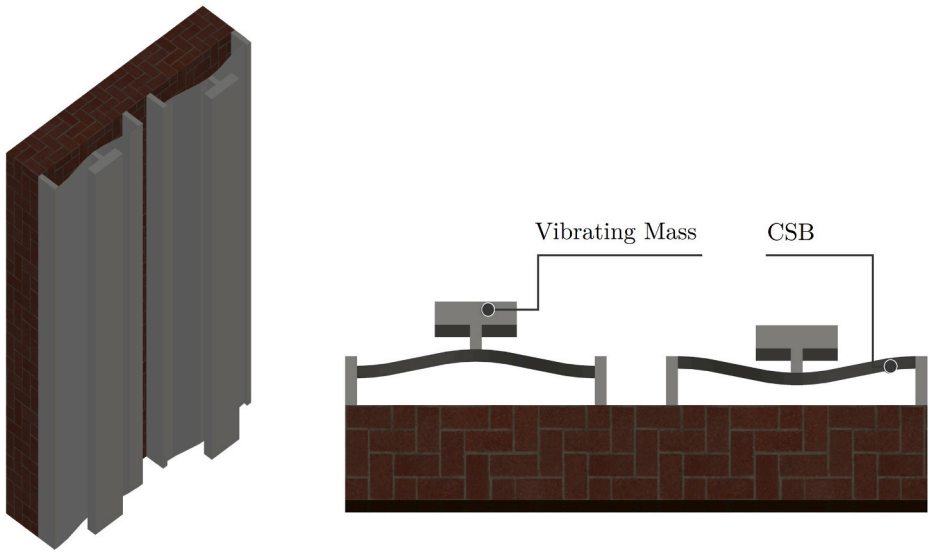

Fig. 1. 3D representation (on the left) and 2D-view (on the right) of the device with indication of the vibrating mass and nonlinear mechanism produced by the CSB.

$y = 0$, for which higher-order contributions are negligible [54], although this assumption should be considered in relation to the specific operating conditions.

From a modelling perspective, under the assumption of negligible mass, the two sides of the CSB, employed in the device as bistable metalayer, are schematised as two inclined springs, each with stiffness k and initial length l_0, attached to a vibrating mass m. Fig. 2 depicts a schematic of the CSB and the corresponding SDoF bistable oscillator, while the typical shape of the potential energy and force–displacement profile is shown in Fig. 3. This simple SDoF formulation considers only displacement in the snap-through direction, however, rotational effects can be directly incorporated in the parameters k_1 and k_3 of the restoring force, since rotations reduce the snapping force and the stiffness in the interwell regime. Distributed mass effect is neglected as the CSB mass is much smaller than the attached vibrating mass, making its contribution negligible.

Also, for reliable parameter estimation, experiments should be properly designed to reproduce a perfectly elastic regime, as the one described in Eqs. (1)-(3). Finally, in case the model cannot be reduced to a SDoF, more complex formulations are needed [55].

3. Bayesian instantaneous identification of nonlinear time-varying parameters

3.1. Statement of the nonlinear identification problem

In the field of identification of nonlinear dynamical systems, an effective methodological approach consists of decoupling the rate-dependent from the rate-independent components as two sequential separate steps [3,56]. In the presence of linear viscous damping, the rate-dependent contribution can be preliminarily identified with classical methods based on free-decay response [3,57–59]. This approach is applicable also to bistable oscillators (with possible generalisation to multi-stable configurations) provided that low-amplitude intrawell oscillations are considered. Then, the main focus of the nonlinear identification task is on the rate-independent component, which characterises the stiffness restoring force governing the potential energy topology and the existence of multi-stable states. The sequential strategy exploits the fact that in the small oscillations of the intrawell regime the prevailing effect is that of viscous damping, unlike the markedly nonlinear response of the interwell regime. This reduces the possibility that the coupled estimation will lead to biased or non-unique solutions. While stiffness coefficients are generally assumed to be time-invariant, this assumption appears restrictive in some real-world cases, especially those involving energy absorption/dissipation [60]. Even though bistable systems are stationary around their equilibrium points, when subject to strong excitations, such as earthquakes, the activation of the snap-through mechanism leads to a non-stationary response [43,61]. As a result, the bistable dynamics in the interwell regime can be effectively described by time-varying parameters, at least for identification purposes. An appealing approach is to assume the signal as a realisation of a process whose statistical properties (mean, variance, higher moments) change slowly over time, thus allowing the parameters to be identified from short analysing windows, i.e. from time-frequency representations [29,62].

Another issue to address is the statistical variability of some characteristics and factors which, especially in bistable systems, can influence the dynamic behaviour and, therefore, the performance of the device [63–65]. In this sense, a Bayesian framework allows model parameters to be treated as random variables and their probability distributions to be updated as new information becomes available [30,36]. Indeed, it is known that, under nonlinear model uncertainty, Bayesian approaches outperform deterministic ones [66]. Both the Bayesian and the intrinsically time-varying approaches, which are desirable for the nonlinear identification procedure of bistable systems, will be discussed in more detail in the following paragraphs.

3.2. Bayesian inference for nonlinear system identification

If a dynamic model of input $u(t)$ and output $y(t)$ is introduced, one may infer a mathematical model describing their relationship (i.e., identification task). In practice, one can refer to a set of observed data of dimension Z, namely $\widetilde{D} = \{(u_i, y_i), i = 1, \cdots, Z\}$, where (u_i, y_i) represents the i-th set of sampled input and output. By considering the parameter vector $\mathbf{p} = \{p_1, p_2, \cdots, p_{N_{par}}\}$, where N_{par} is the total number of parameters describing the dynamic model, a probabilistic estimate of the parameter vector $\mathbf{p}$ may be given by [31]:

$$\widehat{\mathbf{p}} \sim P\left(\mathbf{p} | \widetilde{D}, \mathscr{M}\right) \tag{4}$$

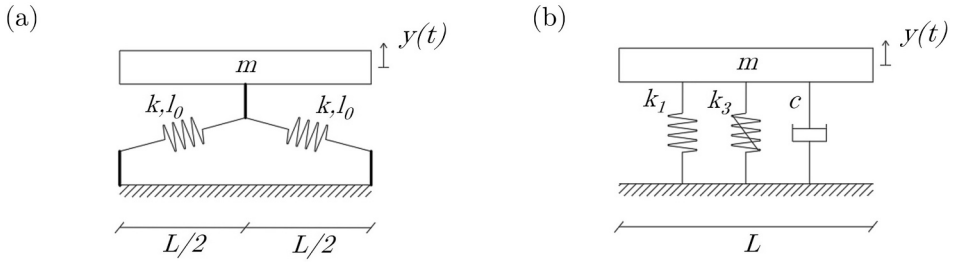

Fig. 2. Schematic of the (a) CSB and the corresponding (b) SDoF bistable oscillator.

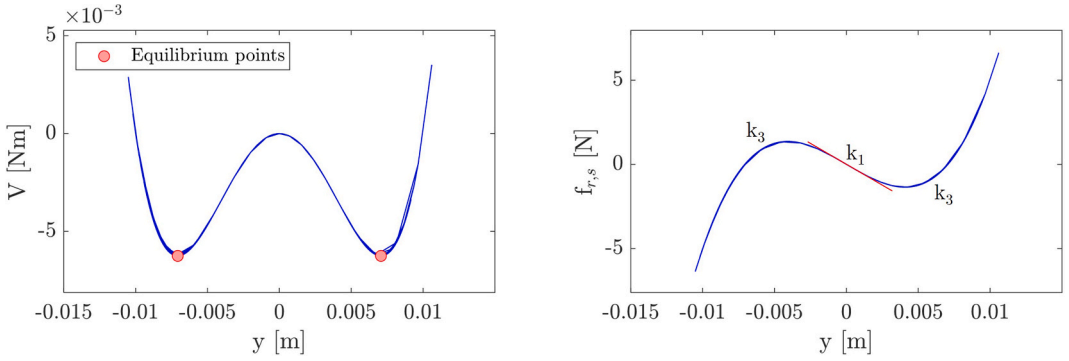

Fig. 3. Potential energy and force–displacement profile of a bistable oscillator with $m = 1$ kg, $k_1 = -5 \times 10^2$ N/m, $k_3 = 1 \times 10^7$ N/m^3, and $c = 10$ Ns/m for a white noise input with null mean and standard deviation equal to 2.

where $\mathscr{M}$ is nothing else than the chosen model, e.g., the one reported in Eq. (2). A classical approach to estimate the probability function P is given by the Bayes one, that basically includes estimating a posterior distribution from a priori probability function of the parameters $\mathbf{p}$ considering the observed data $\widetilde{D}$. The objective is therefore to find a good, and computationally affordable, approximation of the posterior distribution:

$$P\left(\mathbf{p}|\widetilde{D},\mathscr{M}\right) \propto P\left(\widetilde{D}|\mathbf{p},\mathscr{M}\right) P(\mathbf{p}|\mathscr{M}) \tag{5}$$

where the quantities $P\left(\widetilde{D}|\mathbf{p},\mathscr{M}\right)$ and $P(\mathbf{p}|\mathscr{M})$ represent the likelihood of the observed data $\widetilde{D}$ for a given parameter vector $\mathbf{p}$ and the prior distribution over parameter space, respectively. In the ABC algorithm, a good approximation may be given by [67–69]:

$$P\left(\mathbf{p}|\widetilde{D},\mathscr{M}\right) \approx P_\varepsilon\left(\mathbf{p}|\widetilde{D},\mathscr{M}\right) = \int_D g\left(\widetilde{D}|\mathbf{p},\mathscr{M}\right) \mathbf{I}\left(\Delta\left(D,\widetilde{D}\right)\right) P(\mathbf{p}|\mathscr{M}) dD \tag{6}$$

with $\mathbf{I}\left(\Delta\left(D,\widetilde{D}\right)\right)$ as indicator function depending on the distance between the observed and simulated data, $\widetilde{D}$ and D, respectively. The latter can assume the following values:

$$\mathbf{I}\left(\Delta\left(D,\widetilde{D}\right)\right) = \begin{cases} 1 & if \Delta\left(D,\widetilde{D}\right) \leq \varepsilon \\ 0 & if \Delta\left(D,\widetilde{D}\right) > \varepsilon \end{cases} \tag{7}$$

From Eq. (7) it is clear that the ABC algorithm has the main assumption that the distance between the observed and simulated data should be lower than a certain threshold ε. This threshold can be defined by the user, depending on the identification task and on the observed data $\widetilde{D}$. The main advantage of using ABC is that for nonlinear models it might be difficult to formulate an analytical expression of the parameter distribution. Thus, ABC avoids explicit likelihood evaluation by replacing it with simulation-based comparisons between observed and synthetic data, allowing posterior inference without closed-form of likelihoods [36].

3.3. Time-frequency estimator

When the system admits a spectral localisation of its components, an appealing approach to obtain an instantaneous estimate of the parameter vector $\mathbf{p}$ is using time-frequency representations [29]. For a generic signal s, its time-frequency transform $\mathbf{T}_s(t,f)$ allows a simultaneous representation of the signal in the joint time–frequency domain (t,f). In particular, if the signal s takes form of the response of a generic dynamical system, y, possibly described by the parameter vector $\mathbf{p}$, one may minimise the following error function in order to obtain an optimal parameter vector estimate $\mathbf{p}_{\text{opt}}$:

$$\begin{aligned} J(\mathbf{p}) &= \left\| \mathbf{T}_y(t,f;\mathbf{p}) - \widetilde{\mathbf{T}}_y(t,f) \right\| \\ \mathbf{p}_{\text{opt}} &= \arg\left[\min_{\forall \mathbf{p}} J(\mathbf{p}) \right] \end{aligned} \tag{8}$$

with $\widetilde{\mathbf{T}}_y$ and $\mathbf{T}_y$ as the observed and simulated time-frequency transforms of the response y. If the transform is quadratic, Eq. (8) aims to minimise the energy between the two transforms. To preserve the instantaneous energy, one may adapt Eq. (8) to be minimised instant by instant. Therefore, if the excitation is known, for a generic time instant $\bar{t}$ one has:

$$J(\bar{t},\mathbf{p}) = \left\| \mathbf{T}_y(t,f;\mathbf{p}) - \widetilde{\mathbf{T}}_y(t,f) \right\|_{t=\bar{t}}$$

$$\mathbf{p}_{\text{opt}}(\bar{t}) = \arg\left[\min_{\forall \mathbf{p}} J(\bar{t}, \mathbf{p})\right] \tag{9}$$

The choice of the time–frequency transform depends on several factors, such as the possibility of an online implementation, largely discussed in [29]. The spectrogram, which is nothing else than the squared modulus of the STFT, proved to be effective in the identification of nonlinear systems, also in presence of hysteresis and degradation [70]. For a generic stationary process F, the spectrogram can be written as:

$$E\{\text{SPEC}_F^{\gamma}(t,f)\} = \int_{-\infty}^{\infty} |\Gamma(f' - f)|^2 S_F(f') df' \tag{10}$$

where $\Gamma(f)$ is the spectrum of the running window $\gamma(t)$, and $S_F(f)$ is the spectral density associated with the process. One may extended Eq. (10) to locally stationary processes by defining a local spectral density for several stationarity intervals. Hence, the stationarity interval is assumed to match the length of the analysis window $\gamma(t)$ of the STFT and can be used also for signals which are not globally stationary, such as bistable responses. It is worth to specify that the spectrogram estimator of Eq. (10) is a biased estimator, due to the averaging operation. Previous works focused on this bias caused by the analysis window γ [71], also consistently with the time-frequency uncertainty principle, which governs the trade-off between time and frequency resolution in the STFT representation [72]. In this work, a spectrogram has been chosen as time-frequency representation. Thus, by introducing the discrete frequency m and the discrete time n, a possible form of Eq. (9) writes:

$$J(n;\mathbf{p}) = \frac{\sqrt{\frac{1}{M}\sum_{m=0}^{M-1}\left|\text{SPEC}_y^{\gamma}(n,m;\mathbf{p}) - \widetilde{\text{SPEC}}_y^{\gamma}(n,m)\right|^2}}{\sqrt{\frac{1}{M}\sum_{m=0}^{M-1}\left|\widetilde{\text{SPEC}}_y^{\gamma}(n,m)\right|^2}} \tag{11}$$

where SPEC_y^{γ} and $\widetilde{\text{SPEC}}_y^{\gamma}$ are the spectrograms of the simulated and measured response signal y analysed with a running window γ (the dependence on time of the running window has been omitted for brevity's sake) at the time instant $n\Delta t$ and frequency $m\Delta f$.

The objective function J reported in Eq. (11) has traditionally been solved using least squares or optimisation algorithms [70]. In this work, an extension of its solution that accounts for uncertainties by integrating probabilistic approaches is proposed. The main issue is therefore to obtain an instantaneous distribution of the parameter vector $\mathbf{p}$. More specifically, by considering the probabilistic formulation reported in Eqs. (5)–(7), the deterministic optimisation problem of Eq. (11) can be reformulated in terms of the posterior distribution of the parameter vector. Instead of identifying a deterministic optimal parameter vector $\mathbf{p}_{\text{opt}}$, one can obtain a probabilistic estimate of $\mathbf{p}_{\text{opt}}$ at the time instant $\bar{t} = n\Delta t$ as:

$$\widehat{\mathbf{p}}_{\text{opt}}(\bar{t} = n\Delta t) = P_{\varepsilon}\left(\mathbf{p}|\widetilde{D}, \mathscr{M}\right)_{\bar{t}=n\Delta t} \tag{12}$$

where $P_{\varepsilon}\left(\mathbf{p}|\widetilde{D}, \mathscr{M}\right)_{\bar{t}=n\Delta t}$ is nothing more than the posterior distribution calculated with ABC method for a certain threshold ε, see Eq. (6), at the time instant $\bar{t} = n\Delta t$.

3.4. Numerical implementation of the ABC time–frequency estimator

In this section the numerical implementation of the ABC time-frequency estimator is reported. Since it is not possible to obtain a closed solution of Eq. (12), a kernel density estimation (KDE) has been employed to fit the posterior distribution, obtained with ABC, of the optimal parameters $\mathbf{p}_{\text{opt}}$ for each time instant. For any real value of $\mathbf{p}$, the KDE [73] is given by:

$$P_{\varepsilon}\left(\mathbf{p}|\widetilde{D}, \mathscr{M}\right)_{\bar{t}=n\Delta t} \cong \text{KDE}_{\text{post}}(\mathbf{p}) = \frac{1}{N_s b_w}\sum_{j=0}^{N_s-1} K\left(\frac{\mathbf{p} - \mathbf{p}_j}{b_w}\right) \tag{13}$$

where $\mathbf{p}_1, \mathbf{p}_2, \cdots, \mathbf{p}_j, \cdots, \mathbf{p}_{N_s}$ are random sample vectors from an unknown distribution, $K(\bullet)$ is the kernel smoothing function, N_s is the total number of samples, and b_w is the bandwidth of the kernel smoothing window. **Algorithm 1** reports the pseudocode for the implementation of the ABC time-frequency estimator. In this work, **Algorithm 1** has been implemented in Matlab®. The bandwidth b_w has been calculated using the normal approximation method. The threshold ε has been chosen to be a vector composed of decreasing values for the objective function $\mathbf{J}_{thresh}$, in order to refine the search at each optimisation cycle k, according to [68]. In particular, an initially large tolerance threshold is used to avoid low acceptance rates and computational inefficiency, and then it is progressively reduced. In the present work, the tolerance is initialised at $\varepsilon = 1$ and monotonically decreased to $\varepsilon = 0.1$. It is worth nothing that excessively strict tolerance levels were observed to adversely affect the acceptance rate, significantly reducing the goodness of the posterior distribution.

The optimisation has been carried out for a total number of cycles K_{opt} as required from the ABC methods. The convergence criterion for the algorithm was defined by the stabilisation of the posterior distribution to the same shape of the previous cycle. The

parameters have been initially chosen by using a Latin hypercube sampling (LHS) between the minimum and maximum parameter vector $\mathbf{p}_{min}$ and $\mathbf{p}_{max}$.

Algorithm 1 ABC time–frequency estimator.

Threshold objective function vector $\mathbf{J}_{thresh}$
for $n = 1 : N$
  for $k = 1 : K_{opt}$
    $\{\mathbf{p}\}_{j=1}^{N_s} \sim \mathrm{LHS}(\mathbf{p}_{min}, \mathbf{p}_{max})$ — *Generate N_s samples*
    for $j = 1 : N_s$
      Obtain discrete response $y\left(\mathbf{p}_j\right)$ — *From Eq. (2)*
      $\mathrm{SPEC}_y^{\gamma}\left(n, m; \mathbf{p}_j\right) = \left|\mathrm{STFT}_y^{\gamma}\left(n, m; \mathbf{p}_j\right)\right|^2$ — *Compute spectrogram*
      $J_j\left(n; \mathbf{p}_j\right) = \dfrac{\sqrt{\frac{1}{M}\sum_{m=0}^{M-1}\left|\mathrm{SPEC}_y^{\gamma}\left(n, m; \mathbf{p}_j\right) - \widetilde{\mathrm{SPEC}}_y^{\gamma}(n, m)\right|^2}}{\sqrt{\frac{1}{M}\sum_{m=0}^{M-1}\left|\widetilde{\mathrm{SPEC}}_y^{\gamma}(n, m)\right|^2}}$ — *Objective function at frame n*
      $\mathbf{J}(n) = \left[\mathbf{J}(n),\ J_j\left(n; \mathbf{p}_j\right)\right]$
    end
    $\mathbf{J}_{tot}(n) = [\mathbf{J}_{tot}(n),\ \mathbf{J}(n)]$ — *Thresholding*
    if $\mathbf{J}_{tot}(n) < \mathbf{J}_{thresh}(k)$
      $\mathrm{KDE}_{\mathrm{post}}(n; \mathbf{p}) = \dfrac{1}{N_s b_w}\sum_{j=1}^{N_s} K\left(\dfrac{\mathbf{p} - \mathbf{p}_j}{b_w}\right)$ — *Calculate posterior KDE*
    end
  end
end

4. Experimental testing

4.1. Sample description

The first step for setting up the experiments consisted of the design and fabrication of specimens that are able to reproduce the bistable dynamics outlined in Eq. (2). The Bambu Lab X1 Carbon printer (https://bambulab.com/en/x1) was used for this purpose, and the material selected for printing was PLA Basic (https://wiki.bambulab.com/en/filament-acc), a common thermoplastic polyester, due to its ease of processing and relatively low cost [74]. Also, PLA Basic is formulated for high-speed printing, readily supporting print speeds of approximately 250-300 mm/s while exhibiting enhanced toughness and improved interlayer adhesion. Its elastic modulus and density are equal to $E_{PLA} = 2580 \pm 220$ MPa and $\rho_{PLA} = 1240$ kg/m^3. However, it is important to highlight that the actual 3D printing mechanical model performance can be influenced from several factors, including printers, printing conditions, printing models, printing parameters (e.g., infill density), as recently reported in [75]. Given the relatively short duration of each experimental acquisition, i.e., $\ll 60$ s, and the absence of prolonged cyclic loading, viscoelastic degradation and self-heating effects are assumed to be negligible. The sample and its measures are reported in Fig. 4 and in Table 1, respectively.

In order to simulate the bistable behaviour, the sample was designed to be mechanically clamped in a steel support. The support as well its geometric dimensions are reported in Fig. 5.

4.2. Prototype testing machine description

The main issue of experimentally testing bistable systems is the direct measurement of displacements under an applied force, for two main reasons: (i) displacements are the fundamental quantities which describe the jump between the two stable positions; (ii) as a consequence, velocities and accelerations can be easily obtained by differentiation, whereas the inverse process is significantly more prone to numerical errors. Accordingly, the prototype testing machine consists of an electromagnetic actuation system allowing rather precise a priori estimation of the applied force, and very precise optical measurement of displacement via laser system, as shown in Fig. 6(a). The latter employs a HeNe laser (https://www.thorlabs.com) that features a beam of 0.48 mm in diameter and with a power

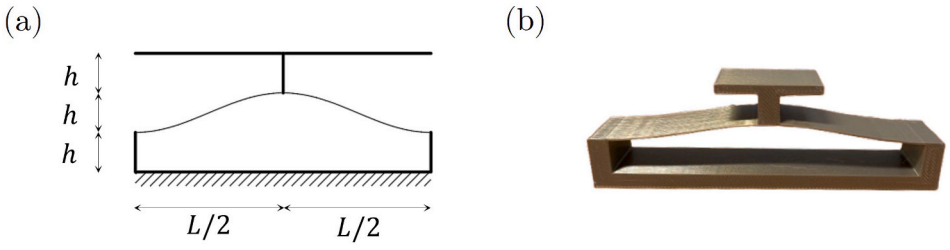

Fig. 4. From schematisation to fabrication: (a) drawing of the CSB and (b) 3D-printed sample.

Table 1
Geometrical values of the 3D-printed CSB.

h[m]	t[m]	L[m]	m[kg]
5×10^{-3}	0.5×10^{-3}	9×10^{-2}	47×10^{-3}

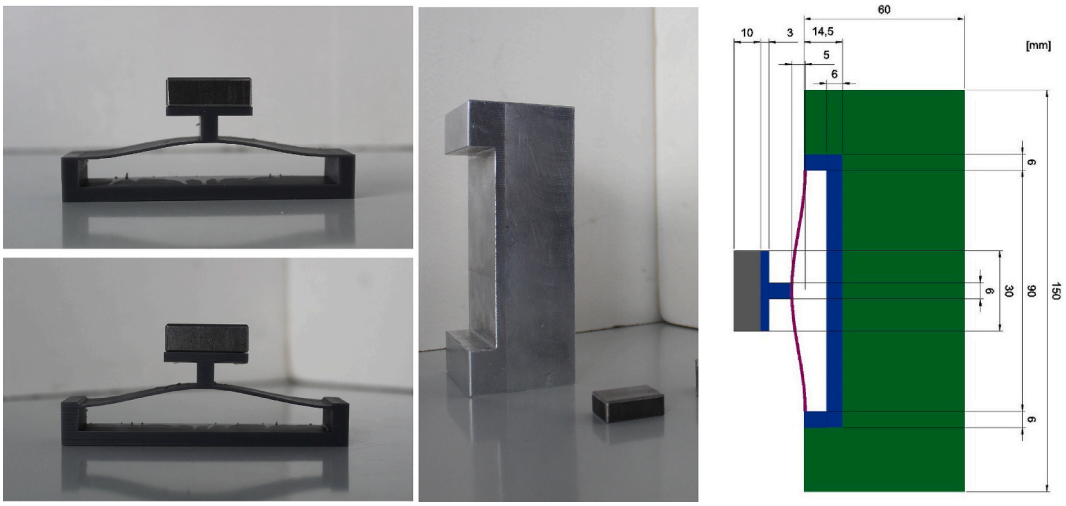

Fig. 5. Bistable sample and its support (dimensions in millimetres).

noise root mean square lower than 1.0%. The laser beam is first focused by a converging cylindrical rod-lens ($\phi = 10$ mm) to make a vertical flat light beam, which is subsequently redirected by two mirrors ($\phi = 25$ mm) at 45° toward a convergent lens (50 × 50 × 5 mm), which focuses the flat beam on a linear position-sensitive detector (PSD), in order to enhance the resolution, see Fig. 6(b).

The displacement is measured by the 12 mm long PSD, which is placed horizontally on the vibrating mass, and detects the position at which the light beam hits the sensitive area, allowing high-precision motion tracking, see Fig. 7(a). When a light spot strikes the PSD, it generates locally an electric charge proportional to the light intensity. This charge flows in both directions as photocurrent through the resistive layer and is extracted at the two opposite output electrodes. The current is divided between the electrodes in inverse proportion to the distance from the incident point, allowing the position to be determined. Considering the thickness of the light blade, the linearity of the PSD, and the noise generated by the dark current of the PSD and the interface electronics, it is possible to conclude that the uncertainty on the calculated position is throughout lower than 50 μm.

On the other hand, the actuation system, rigidly connected to the specimen via a cylindrical plexiglass rod with a diameter of 10 mm, constraints the system against rotation and thus prevents the activation of rotational vibration modes. Under these conditions, the response is dominated by the SDoF oscillator dynamics, as described in Eq. (2). The length of the plexiglass rod is specifically chosen to minimise the magnetic attraction between the steel vibrating mass and the permanent magnets. The actuator itself consists of a cardboard substrate with a copper coil on top and bottom. The copper wire has a diameter of 1 mm, and 20 turns for each side show resistance of 0.2 Ω, see Fig. 7(b). Initially, tracks were added to maintain the position of the actuator. However, due to high friction, it

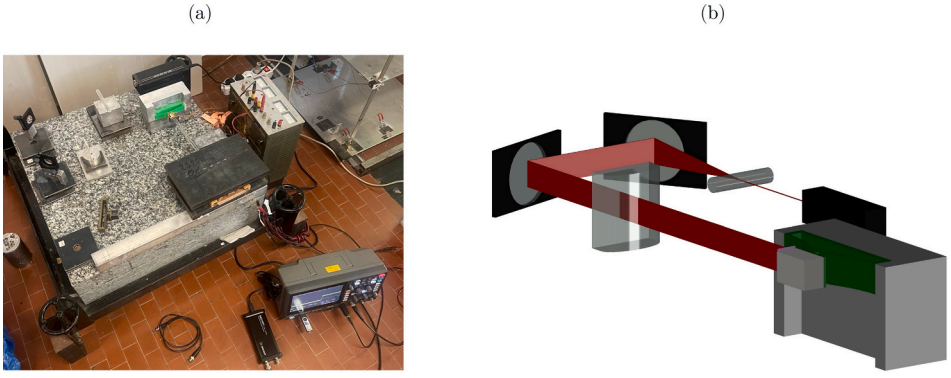

Fig. 6. (a) Prototype testing machine and (b) schematic of the prototype testing setup with focus on the light pattern (in red). (For interpretation of the references to colour in this figure legend, the reader is referred to the web version of this article.)

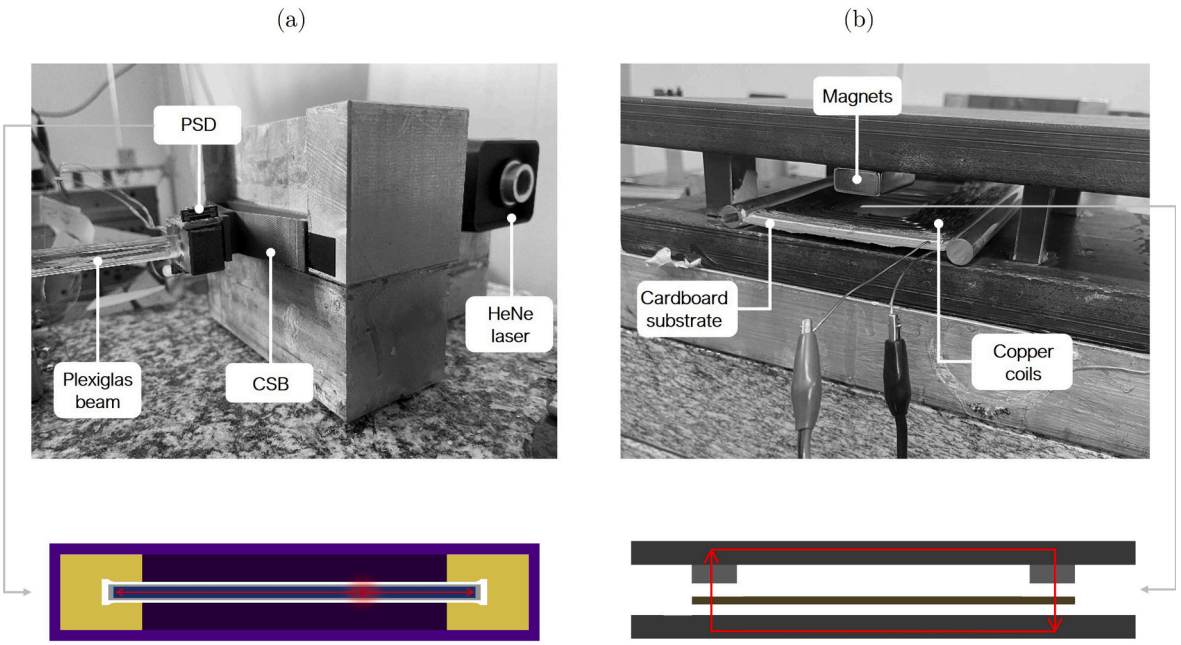

Fig. 7. Significant components in the prototype machine: (a) positioning of PSD with detail on the laser and (b) actuator with focus on the confined magnetic field (depicted in red). (For interpretation of the references to colour in this figure legend, the reader is referred to the web version of this article.)

was decided to remove them and support the actuator with rollers. The force generated by the pusher is produced by the interaction between the current in the coil and the magnetic field of two permanent magnets. A representation of the magnetic circuit is given in Fig. 7(b). It is clear that as designed the magnetic field can be easily confined within the circuit. The extra-strong neodymium (NdFeB) rectangular bar magnets have dimensions of 30 × 10 × 4 mm and a magnetic flux density of 1 T. The apparatus can be used for both free-decay and forced tests. Indeed, the input signal is generated by the function generator embedded in the oscilloscope and is

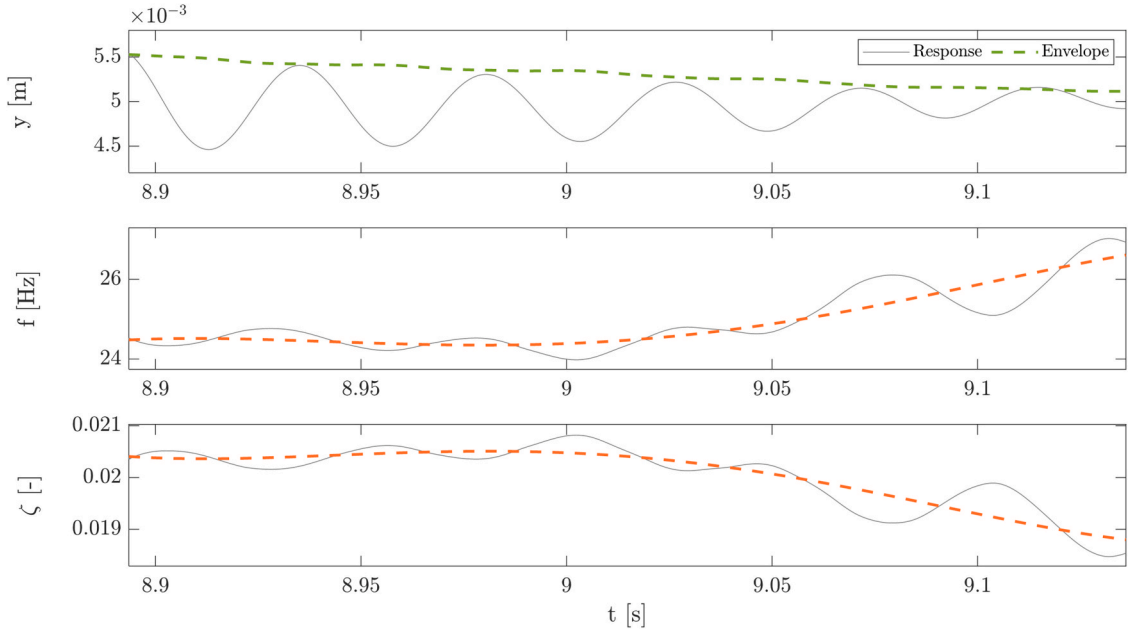

Fig. 8. Identification results of FREEVIB procedure on intrawell free decay oscillations. For what concerns f and ζ, the dashed orange line represents their polynomial trend, while their respective instantaneous estimated values are represented by the continuous light grey line. (For interpretation of the references to colour in this figure legend, the reader is referred to the web version of this article.)

delivered to the actuator through current amplifier capable of a maximum of 20 A. Both systems are anchored on a solid granite base measuring 600 × 600 × 145 mm to ensure stability and vibration isolation. To secure the test specimen, an aluminium fixing support is employed.

5. Results

5.1. Viscous damping characterisation

As a first step, a characterisation of viscous damping, or equivalent viscous damping, related to the rate-dependent dissipation component, was performed to identify one of the most critical parameters of experimental identification. Indeed, the assumption of linear viscous damping may not be fully verified. Furthermore, it should be noted that, even under ideal conditions, identification algorithms can be quite inaccurate; for example, in output-only identification techniques, errors of 20% are common, sometimes even higher depending on the technique used and the stationary conditions [76]. When the bistable system oscillates in intrawell regime, its dynamic parameters can be considered slowly time-varying, and therefore one may consider exploiting the free decay oscillations in order to estimate the instantaneous frequency, and, consequently, instantaneous relative damping. To this aim, the FREEVIB method [77,78] was employed on the free decay response measured after applying an impulsive perturbation to the system when it was at one of the two stable positions.

The instantaneous frequency has been obtained directly from the analytic signal, as described for classical applications of the FREEVIB method. The instantaneous damping ratio has been then obtained from the rate-dependent component $f_{r,d}$, provided by FREEVIB, through a classical least-square fitting [79], as required from [80]. The fitting problem has been solved using the *lsqlin* algorithm in Matlab®, obtaining the instantaneous frequency and damping estimates reported in Fig. 8. As can be observed, both the instantaneous frequency and damping ratio show small oscillations in time. This can be attributed to the nonlinear nature of the intrawell oscillations, corresponding to the case of a monostable Duffing oscillator, which may present multiple components, small in amplitude but high in frequency, besides the principal ones. As a consequence, all the instantaneous functions extracted using Hilbert transform based methods can be classified as fast oscillating functions [81]. In order to highlight the trend of estimation, a third-order polynomial fitting has been carried out for both the instantaneous frequency and damping ratio. As can be observed, for fairly small values of amplitude, the instantaneous damping estimate tends to stabilise to a value of 1.9%.

One of the advantages of using this method is the possibility to obtain a rough estimate of k_1 and k_3 through a least-square fitting starting from the rate-independent component $f_{r,s}$. This allowed the definition of the order of magnitude of the unknown parameters, exploited in the next sections to define the boundaries for more refined time–frequency probabilistic identification task. In particular, the values estimated from FREEVIB are $k_1 = -1.1 \times 10^3$ N/m and $k_3 = 3.6 \times 10^7$ N/m^3.

5.2. Probabilistic estimation of stiffness parameters

After obtaining an estimate of the damping ratio and first trial estimates to initialise the stiffness parameters k_1 and k_3, the ABC time–frequency algorithm reported in **Algorithm 1** was applied to experimental signals to obtain probabilistic estimates of the negative linear stiffness k_1 and the positive cubic stiffness k_3, consistently with the two steps identification strategy discussed in Section 3.1. Since the stiffness coefficients characterise the backbone curve, i.e., the mean force-displacement relationship, they can be identified independently of the damping parameter, which primarily affects the viscous dissipation loop opening. This motivates a sequential two-step estimation procedure. The amplitude of the external excitation $u(t)$ was carefully chosen to ensure the activation of the snap-through mechanism. In practice, a white noise input with null mean and a standard deviation of 5 V was generated at the acquisition system, which was found to be sufficient to overcome the potential barrier and trigger the bistable mechanism governed by

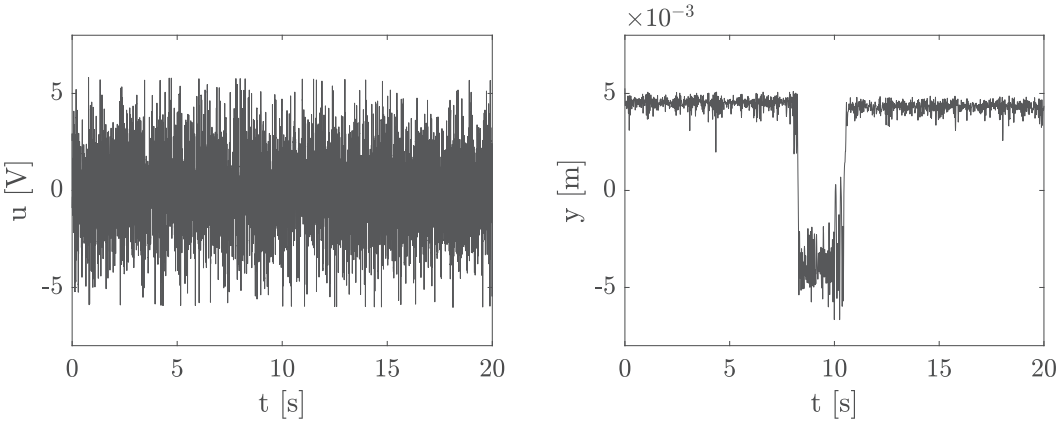

Fig. 9. Input white noise and corresponding displacement response.

the negative linear stiffness k_1, see Fig. 3 for reference. The acquired experimental signals were pre-processed and filtered using a low-pass Butterworth filter of order 2.

Once the pre-processing stage was completed, the Bayesian time–frequency identification procedure detailed in Sections 3.2-3.4 was applied. Specifically, the measured filtered output response and the measured excitation signal were used as the observed dataset $\widetilde{D}$ in the ABC framework. Then, in accordance with Eq. (11), a spectrogram-based estimator was employed to construct the objective function $J(n;\mathbf{p})$, using a Hanning analysis window $\gamma(t)$ (time length: 0.5 s; 90% overlap), to achieve a time–frequency resolution consistent with the characteristic time scales of the interwell regime. Finally, for each time instant a distribution of optimal values, as described by Eqs. (12)-(13), has been obtained independently for k_1 and k_3. Within the ABC formulation, experimental uncertainties are not explicitly modelled, but are accounted for into the posterior distribution through the objective function $J(n;\mathbf{p})$ between simulated and measured responses. The input and output signals used for identification are reported in Fig. 9 for reference. The values reported in Table 2 were used for the estimation procedure. The results are reported in Fig. 10.

Fig. 10 shows that the parameter k_1 has a statistical mode, i.e., the most frequent value in a distribution, of nearly -1×10^3 N/m for every time instant considered, leading to a confirmation of what already achieved with the FREEVIB procedure. On the other hand, the parameter k_3, governing the intrawell oscillation, shows a higher value with respect to the one used for the initialisation of the procedure, with a statistical mode value of 6.7×10^7 N/m^3. This discrepancy is consistent with the excitation level selected for the experiments, which was calibrated to activate snap-through between the two stable equilibrium points. Indeed, in the interwell regime, the response is primarily controlled by the negative linear stiffness term k_1, whereas the positive cubic stiffness k_3 mainly affects the local curvature of the potential within each well. A dispersion of both parameters can be observed in Fig. 10(b)–(d) during snap-through events, where the response is markedly non-stationary. Nevertheless, the proposed approach demonstrates robustness, especially considering the intrinsic difficulty of identifying nonlinear parameters in non-stationary responses.

Although not reported here for brevity, additional tests on synthetic data generated under zero-mean white noise with a standard deviation of 5, using parameters obtained from the experimental identification procedure, provided consistent results, supporting the robustness of the proposed algorithm. It is worth noting that the proposed identification algorithm may encounter higher computational costs with respect to traditional Bayesian filters, while showing favourable performance in markedly nonlinear and time-varying systems, especially in experimental settings.

A second identification task, relevant to the functioning of the device, involved the case of the system under earthquake excitation. The L'Aquila earthquake (https://www.ont.ingv.it/) scaled at 5 V was chosen as input excitation. The acquired experimental signals were pre-processed as in the case of white noise excitation. The earthquake as well as the output response of the system are reported in Fig. 11. Table 3 reports the values used for the identification, while Fig. 12 shows the estimation results.

Again, both the negative linear stiffness k_1 and the positive cubic stiffness k_3 are accurately identified under seismic excitation. The estimate of the negative linear stiffness k_1 appears significantly more stable than that of the positive cubic stiffness k_3, further reflecting the predominant role of k_1 in governing the interwell response.

A comparison between Fig. 10 and Fig. 12 reveals that the magnitude of the negative linear stiffness k_1 identified under seismic excitation, with a statistical mode value of -2.1×10^3 N/m, is approximately twice as large as the corresponding estimate obtained under white noise, with a statistical mode value of -1×10^3 N/m. This discrepancy reflects the influence of the excitation characteristics on the bistable mechanism. Of particular interest for this research, in bistable systems larger negative values of k_1 can be related to improved dissipation properties [82]. Consequently, from a quantitative standpoint, the higher magnitude of k_1 observed under seismic excitation is expected to result in higher values of dissipated energy. The dissipation efficiency of the device under distinct types of excitations will be further discussed in Section 6.

6. Discussion on the efficiency of the device

As stated in Section 5.2, the identification of k_1 and k_3 was performed independently. This decoupling is supported by the different roles of k_1 and k_3 in the bistable dynamics, predominantly governing the interwell and the intrawell responses, respectively. Moreover, this allows the mitigation of the computational burden of multidimensional Bayesian inference [83,84]. This led to an independent mono-dimensional distribution for each of the parameter. However, in order to calculate the dissipated energy, one should consider a bi-dimensional distribution of the parameters pair (k_1,k_3). In particular, 1000 samples of k_1 and k_3 were extracted from the corresponding mono-dimensional distributions (reported in Fig. 10 and Fig. 12). A bi-dimensional distribution was then fitted according to Eq. (13) over a grid of parameters $[k_1,k_3]$ sampled with LHS. From this bi-dimensional distribution, 200 samples of the couple (k_1,k_3) were extracted and used for the resolution of the differential equation of Eq. (2) employing ODE45 solver in Matlab®. It is worth noting that the dissipated energy is mainly associated with the high-velocities occurring during interwell transitions, where the influence of k_1

Table 2
Values of the parameters used for the identification procedure under white noise.

Parameter	Initial value	Lower boundary	Upper boundary
m[kg]	47×10^{-3}	Fixed	Fixed
ζ[−]	1.9×10^{-2}	Fixed	Fixed
k_1[N/m]	-1.1×10^3	-2.2×10^3	0
k_3[N/m^3]	3.6×10^7	0	9.0×10^7

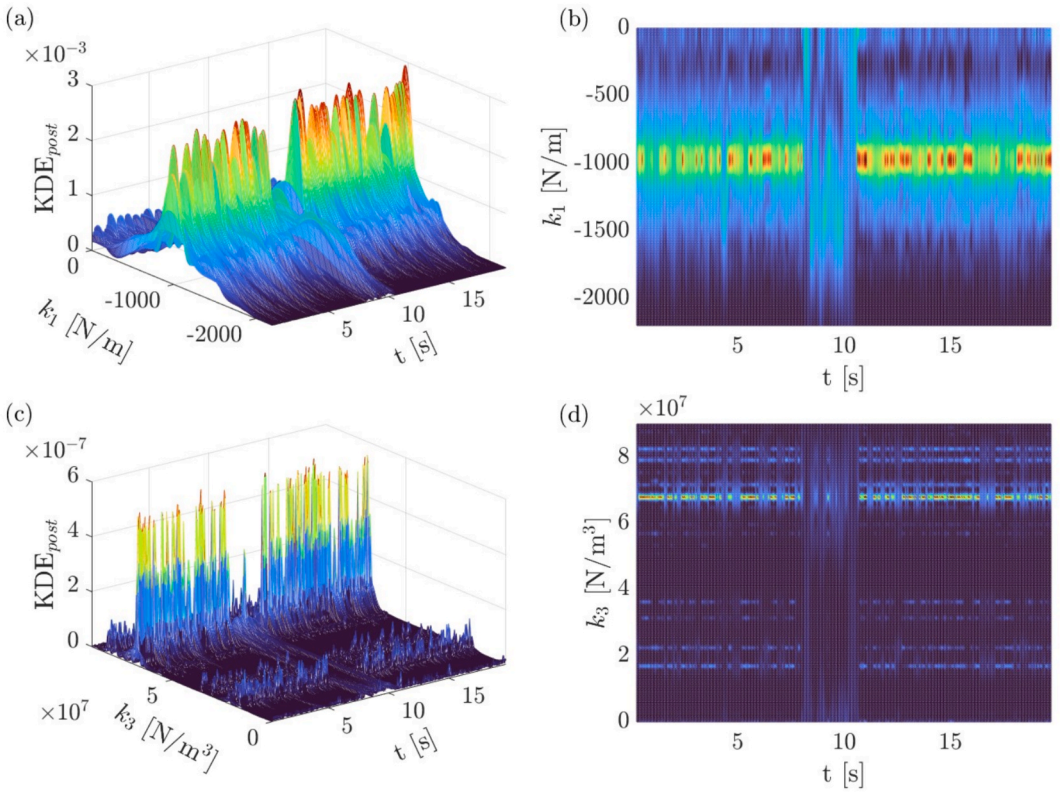

Fig. 10. Identification results under white noise: 3D view of the posterior kernel density estimated for k_1 (a) and k_3 (c), and top view of the tracking of the statistical mode during time of k_1 (b) and k_3 (d).

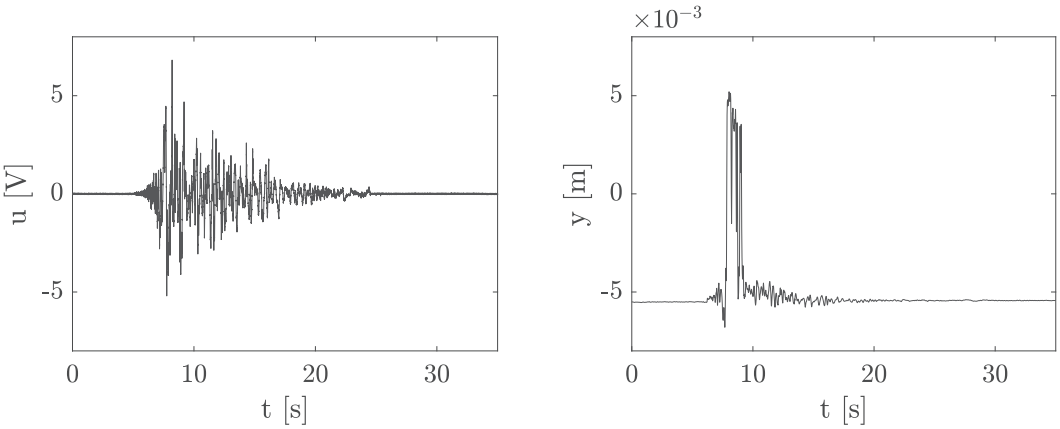

Fig. 11. Input earthquake and corresponding displacement response.

Table 3
Values of the parameters used for the identification procedure under seismic excitation.

Parameter	Initial value	Lower boundary	Upper boundary
m[kg]	47×10^{-3}	Fixed	Fixed
ζ[−]	1.9×10^{-2}	Fixed	Fixed
k_1[N/m]	-1.1×10^{3}	-8.2×10^{3}	0
k_3[N/m^3]	3.6×10^{7}	0	2.6×10^{8}

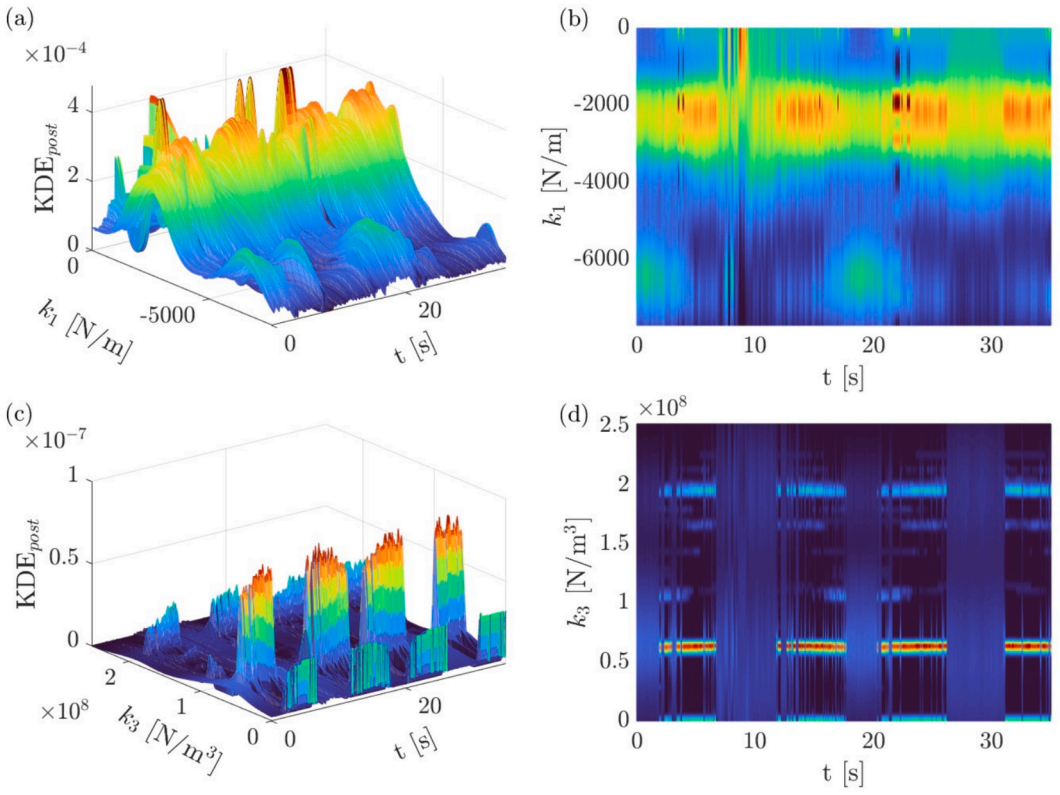

Fig. 12. Identification results under seismic excitation: 3D view of the posterior kernel density estimated for k_1 (a) and k_3 (c), and top view of the tracking of the statistical mode value during time of k_1 (b) and k_3 (d).

is expected to be more impacting. Finally, the dissipated energy $E_{d,cum}$ was calculated as a cumulative function over time as:

$$E_{d,cum}(t) = 2\zeta\omega_n m_T \int_0^t \dot{y}(t)^2 dt \tag{14}$$

In Eq. (14), ζ is the damping ratio, as identified in Section 5.1, ω_n is the circular frequency, derived from the natural frequency f_n identified in Section 5.1, and m_T is the total mass of the system, calculated as the sum of the mass of the actuator and the mass of the bistable sample, obtainable from the geometric dimensions and material properties of Section 4.1. The velocity response of the system,

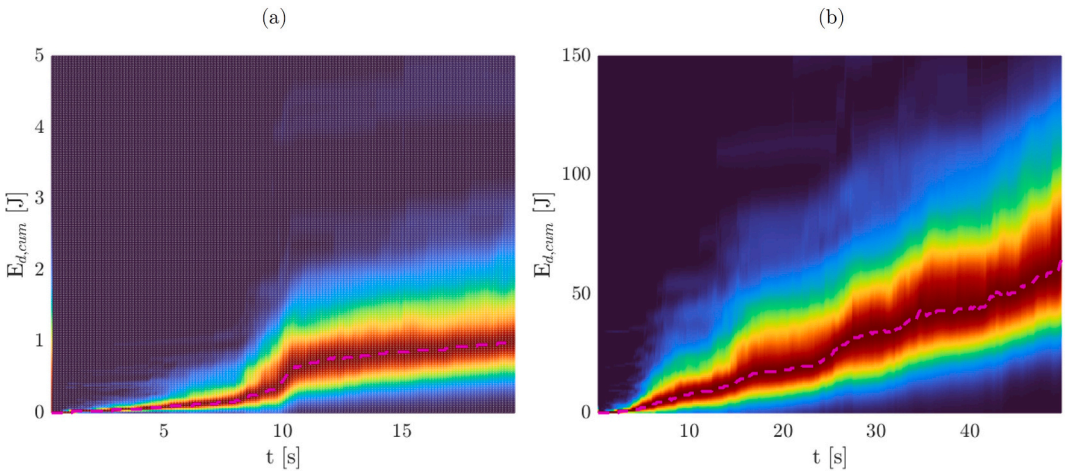

Fig. 13. Cumulative dissipated energy under (a) white noise and (b) earthquake excitation and its mean value (pink dashed line). (For interpretation of the references to colour in this figure legend, the reader is referred to the web version of this article.)

$\dot{y}(t)$, is retrieved from the numerical integration of Eq. (2). Finally, the values of $E_{d,cum}$ were fitted as KDE. The process was repeated for the two external excitations considered, i.e., white noise and L'Aquila earthquake. Results for both input excitations are reported in Fig. 13.

In the case of white noise, one single step around 10 s is observable and a statistical mode value of around 1 J represents the maximum energy reachable under this kind of dissipation; in the case of the earthquake, there are several steps over time, given that the strong non-stationarity of the signal leads to successive snap-through events, up to a dissipated energy of 64.82 J, that is more than 60 times the value obtained with white noise.

It is important to highlight that, since the dashed pink line represents a statistical mode value, the confidence bounds should be carefully evaluated. In this respect, a difference in the confidence bounds of the dissipated energy is observable for the two excitations: the energy dissipated under seismic excitation presents larger confidence bounds (given by the red area and delimitated by the smaller green area) than the white noise case. This may be ascribed to the larger uncertainty of the parameters k_1 and k_3 in the identification task.

To more directly quantify the dissipation efficiency of the device, an equivalent linearisation can be conducted to determine an equivalent damping ratio ζ_{eq}, which is in general amplitude dependent. In particular, here the definition of ζ_{eq} is supported by experimental evidence obtained under white noise excitation. Fig. 14 shows the stiffness restoring force $f_{r,s}$ for intrawell and interwell oscillations. In particular, from Fig. 14(a) it is intuitive that the cycle shape evolves with respect to the oscillation amplitude. More specifically, Fig. 14(b–c) represent the specific shape for intrawell and interwell responses. In the case of low-amplitude oscillations, the oscillations are mainly viscoelastic, attributable to a nearly elliptical shape, consistent with a viscoelastic behaviour. Conversely, the large-amplitude oscillations are characterised by a closed area, primarily due bistable mechanism.

The above-mentioned equivalent damping ratio ζ_{eq} represents a cumulative measure of how much energy the device extracts from the system with respect to the potential energy E_p [85] and can be calculated on the basis of the several cycles observed during intrawell and interwell oscillations. Accordingly, it can be defined for each time instant t_c, corresponding to the central time of the cycle, as [85]:

$$\zeta_{eq}(t_c) = \frac{1}{4\pi}\frac{E_{d,c}}{E_p} \tag{15}$$

where $E_{d,c}$ is the dissipated energy per cycle, corresponding to the subtended area of the cycle shape, and E_p is the potential energy calculated as [86]:

$$E_p = \frac{1}{2}k_{eq}h^2 \tag{16}$$

with h as height of the CSB (for reference see Fig. 4), and k_{eq} as equivalent stiffness, calculated as:

$$k_{eq} = \frac{\int_{-h}^{h} k_t dy}{2h} \tag{17}$$

where k_t is the tangent stiffness, directly obtainable from k_1 and k_3. Fig. 15 shows the evolution in time of ζ_{eq} in the case of earthquake excitation, for which the device effectiveness should be assessed. While for low-amplitudes oscillations the values of ζ_{eq} are aligned with the 1.9% value obtained from the FREEVIB identification, a significant increase in damping, reaching a value of 6%, can be observed in proximity of the snap-through phenomenon, corresponding to a jump in the displacement response. These higher values of ζ_{eq} are attributable to the presence of the negative linear stiffness k_1 in bistable systems [85], also in accordance with the slightly increased value of k_1 experimentally identified under earthquake excitation.

7. Conclusions

This work presented a novel probabilistic instantaneous identification technique for nonlinear systems characterised by uncertainty in parameters. To this end, an estimator combining time-frequency and probabilistic approaches, in particular ABC, was proposed. The estimation was validated experimentally on the signals recorded from a laboratory testing on a 3D-printed bistable sample, engineered for seismic energy dissipation. It is worth noting that for this purpose a special testing machine was used, designed, and built specifically for this type of dynamic testing on bistable systems. The conclusions of the works are outlined hereinafter:

- The backbone curve was shown to be independent of viscous dissipation, confirming that stiffness parameters can be identified independently of damping, which primarily governs dissipation loop opening.
- The identification proved robust under different types of excitations. The observed dispersion in parameter estimates during snap-through events reflects the combined effects of non-stationarity and the window resolution required by the adopted algorithm.
- The measured instantaneous energy demonstrated the effectiveness of the bistable device, which represents a critical aspect in real-world applications.
- Under earthquake excitation, the device showed an increased efficiency in terms of ζ when entering interwell oscillations with respect to low-amplitude case, i.e., intrawell, oscillations.

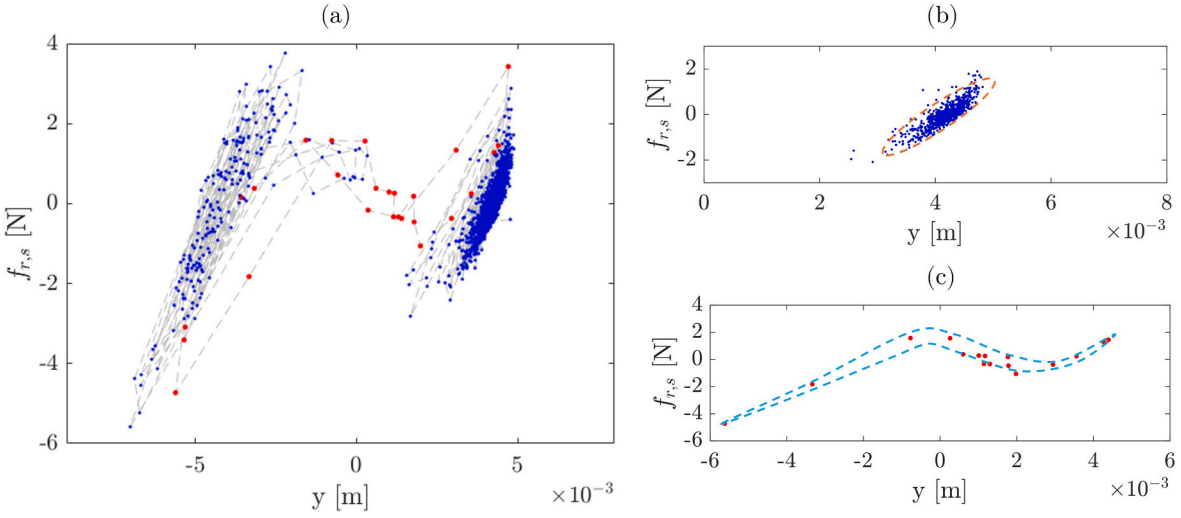

Fig. 14. (a) Stiffness restoring force vs. displacement: total nonlinear $f_{r,s}$ (in dashed light grey), intrawell $f_{r,s}$ (in blue), and interwell $f_{r,s}$ (in red). Representation of the theoretical specific shape of the cycle for (b) intrawell, in light orange, and (c) interwell, in light blue, oscillations. (For interpretation of the references to colour in this figure legend, the reader is referred to the web version of this article.)

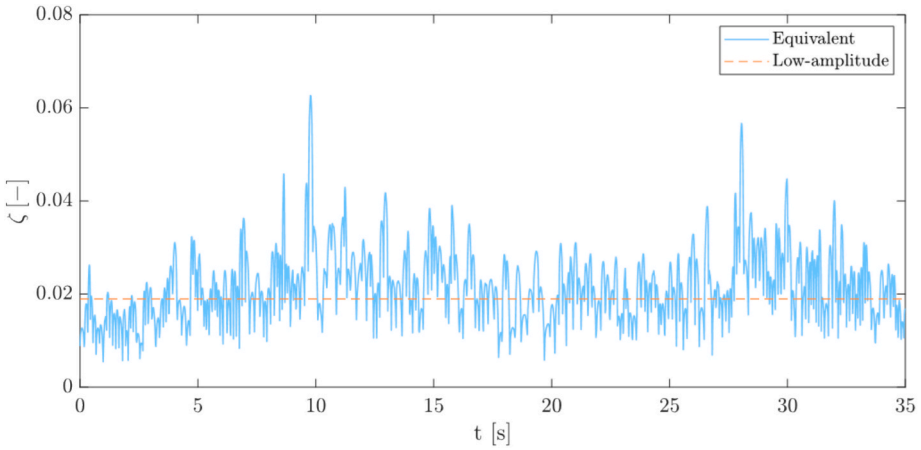

Fig. 15. Equivalent damping ratio under earthquake excitation and estimated low-amplitude damping ratio from FREEVIB procedure.

Future research will focus on the study of different bistable configurations, in order to increase the efficiency of the system and its ability to dissipate energy under seismic actions.

CRediT authorship contribution statement

L. Scussolini: Writing – original draft, Visualization, Validation, Software, Methodology, Investigation, Formal analysis, Data curation, Conceptualization. **V. Cavanni:** Writing – original draft, Visualization, Validation, Software, Methodology, Investigation, Formal analysis, Data curation, Conceptualization. **G. Miraglia:** Writing – review & editing, Visualization, Validation, Software, Methodology, Investigation, Data curation, Conceptualization. **A. De Marchi:** Writing – review & editing, Visualization, Validation, Methodology, Investigation, Data curation, Conceptualization. **R. Ceravolo:** Writing – review & editing, Visualization, Validation, Supervision, Project administration, Methodology, Investigation, Funding acquisition, Data curation, Conceptualization.

Declaration of competing interest

The authors declare that they have no known competing financial interests or personal relationships that could have appeared to influence the work reported in this paper.

Acknowledgments

This publication is part of the project PNRR-NGEU, which has received funding from the MUR-DM 118/2023. The research was supported by Fondazione Compagnia di San Paolo, OPTIMISE project, call TRAPEZIO – Paving the way to research excellence and talent.

Data availability

Data will be made available on request.

References

[1] X. Hong, R.J. Mitchell, S. Chen, C.J. Harris, K. Li, G.W. Irwin, Model selection approaches for non-linear system identification: a review, Int. J. Syst. Sci. 39 (2008) 925–946, https://doi.org/10.1080/00207720802083018.
[2] K. Milkova, E. Dumova-Jovanoska, Methodology for seismic vulnerability assessment of pre-code masonry buildings using region-specific data, Civil Eng. J. 11 (2025).
[3] Q. Liu, Y. Zhang, Z. Hou, Y. Qiao, J. Cao, Y. Lei, Optimal Hilbert transform parameter identification of bistable structures, Nonlinear Dyn. 111 (2023) 5449–5468, https://doi.org/10.1007/s11071-022-08120-z.
[4] Q. Liu, J. Cao, Y. Zhang, Z. Zhao, G. Kerschen, X. Jing, Interpretable sparse identification of a bistable nonlinear energy sink, Mech. Syst. Sig. Process. 193 (2023) 110254, https://doi.org/10.1016/j.ymssp.2023.110254.
[5] H. Vinod Varma, in: Numerical Methods for Parameter Estimation in Dynamical Systems Using Measurements at Bifurcation Points, 2025, https://doi.org/10.11588/HEIDOK.00036853.
[6] R. Zhu, S. Marchesiello, D. Anastasio, D. Jiang, Q. Fei, Nonlinear system identification of a double-well Duffing oscillator with position-dependent friction, Nonlinear Dyn. 108 (2022) 2993–3008, https://doi.org/10.1007/s11071-022-07346-1.
[7] X. Yu, J. Zhou, H. Liang, Z. Jiang, L. Wu, Mechanical metamaterials associated with stiffness, rigidity and compressibility: a brief review, Prog. Mater Sci. 94 (2018) 114–173, https://doi.org/10.1016/j.pmatsci.2017.12.003.
[8] S. Dalela, P.S. Balaji, D.P. Jena, A review on application of mechanical metamaterials for vibration control, Mech. Adv. Mater. Struct. 29 (2022) 3237–3262, https://doi.org/10.1080/15376494.2021.1892244.
[9] S. Shan, S.H. Kang, J.R. Raney, P. Wang, L. Fang, F. Candido, J.A. Lewis, K. Bertoldi, Multistable architected materials for trapping elastic strain energy, Adv. Mater. 27 (2015) 4296–4301, https://doi.org/10.1002/adma.201501708.
[10] S. Chen, X. Tan, J. Hu, S. Zhu, B. Wang, L. Wang, Y. Jin, L. Wu, A novel gradient negative stiffness honeycomb for recoverable energy absorption, Compos. B Eng. 215 (2021) 108745, https://doi.org/10.1016/j.compositesb.2021.108745.
[11] D.M.J. Dykstra, C. Lenting, A. Masurier, C. Coulais, Buckling metamaterials for extreme vibration damping, Adv. Mater. 35 (2023) 2301747, https://doi.org/10.1002/adma.202301747.
[12] J.P. Noël, G. Kerschen, Nonlinear system identification in structural dynamics: 10 more years of progress, Mech. Syst. Sig. Process. 83 (2017) 2–35, https://doi.org/10.1016/j.ymssp.2016.07.020.
[13] G. Quaranta, W. Lacarbonara, S.F. Masri, A review on computational intelligence for identification of nonlinear dynamical systems, Nonlinear Dyn. 99 (2020) 1709–1761, https://doi.org/10.1007/s11071-019-05430-7.
[14] G. Kerschen, K. Worden, A.F. Vakakis, J.-C. Golinval, Past, present and future of nonlinear system identification in structural dynamics, Mech. Syst. Sig. Process. 20 (2006) 505–592, https://doi.org/10.1016/j.ymssp.2005.04.008.
[15] C.M. Richards, R. Singh, Identification of multi-degree-of-freedom non-linear systems under random excitations by the "reverse path" spectral method, J. Sound Vib. 213 (1998) 673–708, https://doi.org/10.1006/jsvi.1998.1522.
[16] S.A. Billings, in: Nonlinear System Identification: NARMAX Methods in the Time, Frequency, and Spatio–Temporal Domains, 1st ed., Wiley, 2013 https://doi.org/10.1002/9781118535561.
[17] H.J. Rice, J.A. Fitzpatrick, A procedure for the identification of linear and non-linear multi-degree-of-freedom systems, J. Sound Vib. 149 (1991) 397–411, https://doi.org/10.1016/0022-460X(91)90444-O.
[18] G.H. Golub, C.F. Van Loan, An analysis of the total least squares problem, SIAM J. Numer. Anal. 17 (1980) 883–893, https://doi.org/10.1137/0717073.
[19] R. Fletcher, in: Practical Methods of Optimization, 1st ed., Wiley, 2000 https://doi.org/10.1002/9781118723203.
[20] M.I. Ribeiro, Kalman and Extended Kalman Filters: Concept, Derivation and Properties, (n.d.).
[21] M. Wu, A.W. Smyth, Application of the unscented Kalman filter for real-time nonlinear structural system identification, Struct. Control Health Monit. 14 (2007) 971–990, https://doi.org/10.1002/stc.186.
[22] M. Feldman, Non-linear system vibration analysis using Hilbert transform–I. Free vibration analysis method "Freevib", in: Mechanical Systems and Signal Processing, 1994, pp. 119–127, https://doi.org/10.1006/mssp.1994.1011.
[23] M. Feldman, Non-linear system vibration analysis using Hilbert transform–II. Forced vibration analysis method "Forcevib", in: Mechanical Systems and Signal Processing, 1994, pp. 309–318, https://doi.org/10.1006/mssp.1994.1023.
[24] N.E. Huang, Z. Shen, S.R. Long, M.C. Wu, H.H. Shih, Q. Zheng, N.-C. Yen, C.C. Tung, H.H. Liu, The empirical mode decomposition and the Hilbert spectrum for nonlinear and non-stationary time series analysis, in: Proceedings of the Royal Society of London. Series A: Mathematical, Physical and Engineering Sciences, 1998, pp. 903–995.
[25] A.A. Galatage, S.B. Patil, Seismic assessment of first and second secant stiffness for the masonry infilled RC frame, Civ. Eng. J. 11 (2025) 472–487, https://doi.org/10.28991/CEJ-2025-011-02-05.
[26] F. Mandita, A. Ashari, M.E. Wibowo, W. Suryanto, Hybrid time series methods and machine learning for seismic analysis and volcano eruption predict, HighTech. Innov. J. 6 (2025) 104–122.
[27] P. Bonato, R. Ceravolo, A. De Stefano, F. Molinari, Use of cross-time–frequency estimators for structural identification in non-stationary conditions and under unknown excitation, J. Sound Vib. 237 (2000) 775–791, https://doi.org/10.1006/jsvi.2000.3097.
[28] Z. Feng, M. Liang, F. Chu, Recent advances in time–frequency analysis methods for machinery fault diagnosis: a review with application examples, Mech. Syst. Sig. Process. 38 (2013) 165–205, https://doi.org/10.1016/j.ymssp.2013.01.017.
[29] R. Ceravolo, Time–Frequency Analysis, in: C. Boller, F. Chang, Y. Fujino (Eds.), Encyclopedia of Structural Health Monitoring, 1st ed., Wiley, 2008 https://doi.org/10.1002/9780470061626.shm047.
[30] J.L. Beck, L.S. Katafygiotis, Updating Models and Their Uncertainties. I: Bayesian Statistical Framework, J. Eng. Mech. 124 (1998) 455–461, https://doi.org/10.1061/(ASCE)0733-9399(1998)124:4(455).
[31] P.L. Green, K. Worden, Bayesian and Markov chain Monte Carlo methods for identifying nonlinear systems in the presence of uncertainty, Phil. Trans. R. Soc. A 373 (2015) 20140405, https://doi.org/10.1098/rsta.2014.0405.
[32] D. Luengo, L. Martino, M. Bugallo, V. Elvira, S. Särkkä, A survey of Monte Carlo methods for parameter estimation, EURASIP J. Adv. Signal Process. 2020 (2020) 25, https://doi.org/10.1186/s13634-020-00675-6.
[33] T.B. Schön, F. Lindsten, J. Dahlin, J. Wågberg, C.A. Naesseth, A. Svensson, L. Dai, Sequential Monte Carlo Methods for System Identification**This work was supported by the projects Learning of complex dynamical systems (Contract number: 637-2014-466) and Probabilistic modeling of dynamical systems (Contract

number: 621-2013-5524), both funded by the Swedish Research Council, IFAC-PapersOnLine 48 (2015) 775–786, https://doi.org/10.1016/j.ifacol.2015.12.224.
[34] K. Worden, J.J. Hensman, Parameter estimation and model selection for a class of hysteretic systems using Bayesian inference, Mech. Syst. Sig. Process. 32 (2012) 153–169, https://doi.org/10.1016/j.ymssp.2012.03.019.
[35] A. Ben Abdessalem, N. Dervilis, D. Wagg, K. Worden, Model selection and parameter estimation in structural dynamics using approximate Bayesian computation, Mech. Syst. Sig. Process. 99 (2018) 306–325, https://doi.org/10.1016/j.ymssp.2017.06.017.
[36] Y. Huang, C. Shao, B. Wu, J.L. Beck, H. Li, State-of-the-art review on Bayesian inference in structural system identification and damage assessment, Adv. Struct. Eng. 22 (2019) 1329–1351, https://doi.org/10.1177/1369433218811540.
[37] K. Erazo, S. Nagarajaiah, An offline approach for output-only Bayesian identification of stochastic nonlinear systems using unscented Kalman filtering, J. Sound Vib. 397 (2017) 222–240, https://doi.org/10.1016/j.jsv.2017.03.001.
[38] D. Ding, K.F. He, W.Q. Qian, A Bayesian adaptive unscented kalman filter for aircraft parameter and noise estimation, J. Sens. 2021 (2021) 9002643, https://doi.org/10.1155/2021/9002643.
[39] T.G. Ritto, S. Beregi, D.A.W. Barton, Reinforcement learning and approximate Bayesian computation (RL-ABC) for model selection and parameter calibration of time-varying systems, Mech. Syst. Sig. Process. 200 (2023) 110458, https://doi.org/10.1016/j.ymssp.2023.110458.
[40] A. Jasra, S.S. Singh, J.S. Martin, E. McCoy, Filtering via approximate Bayesian computation, Stat. Comput. 22 (2012) 1223–1237, https://doi.org/10.1007/s11222-010-9185-0.
[41] K.-V. Yuen, S.-C. Kuok, Online updating and uncertainty quantification using nonstationary output-only measurement, Mech. Syst. Sig. Process. 66 (2016) 62–77.
[42] M.B. Priestley, Evolutionary spectra and non-stationary processes, J. Roy. Stat. Soc.: Ser. B (Methodol.) 27 (1965) 204–229.
[43] C. Cheng, A. Sa-Ngasoongsong, O. Beyca, T. Le, H. Yang, Z. James Kong, S.T.S. Bukkapatnam, Time series forecasting for nonlinear and non-stationary processes: a review and comparative study, IIE Trans. 47 (2015) 1053–1071, https://doi.org/10.1080/0740817X.2014.999180.
[44] Y. Chen, W. Su, S. Tesfamariam, Z. Qian, W. Zhao, Z. Yang, F. Zhou, Experimental study of magnetic bistable nonlinear energy sink for structural seismic control, Soil Dyn. Earthq. Eng. 164 (2023) 107572, https://doi.org/10.1016/j.soildyn.2022.107572.
[45] H. Zuo, S. Zhu, Bistable track nonlinear energy sinks with nonlinear viscous damping for impulsive and seismic control of frame structures, Eng. Struct. 272 (2022) 114982, https://doi.org/10.1016/j.engstruct.2022.114982.
[46] A.F. Vakakis, O.V. Gendelman, L.A. Bergman, A. Mojahed, M. Gzal, Nonlinear targeted energy transfer: state of the art and new perspectives, Nonlinear Dyn. 108 (2022) 711–741, https://doi.org/10.1007/s11071-022-07216-w.
[47] K. Csilléry, M.G.B. Blum, O.E. Gaggiotti, O. François, Approximate Bayesian Computation (ABC) in practice, Trends Ecol. Evol. 25 (2010) 410–418, https://doi.org/10.1016/j.tree.2010.04.001.
[48] M. Leon, M.L. Woods, A.J. Fedorec, C.P. Barnes, A computational method for the investigation of multistable systems and its application to genetic switches, BMC Syst. Biol. 10 (2016) 130.
[49] T. Pinkaew, P. Lukkunaprasit, P. Chatupote, Seismic effectiveness of tuned mass dampers for damage reduction of structures, Eng. Struct. 25 (2003) 39–46.
[50] T.T. Soong, G.F. Dargush, Passive energy dissipation systems in structural engineering, (No Title) (1997).
[51] M. Parseh, M. Dardel, M.H. Ghasemi, Performance comparison of nonlinear energy sink and linear tuned mass damper in steady-state dynamics of a linear beam, Nonlinear Dyn. 81 (2015) 1981–2002.
[52] G. Habib, F. Romeo, Comparative analysis of NES and TMD performance via high-dimensional invariant manifolds, in: IUTAM Symposium on Exploiting Nonlinear Dynamics for Engineering Systems, 2018, pp. 143–153.
[53] X. Tan, B. Wang, L. Wang, S. Zhu, S. Chen, K. Yao, P. Xu, Effect of beam configuration on its multistable and negative stiffness properties, Compos. Struct. 286 (2022) 115308, https://doi.org/10.1016/j.compstruct.2022.115308.
[54] R.L. Harne, K.-W. Wang, Harnessing bistable structural dynamics: for vibration control, energy harvesting and sensing, John Wiley & Sons, 2017.
[55] H. Hussein, M.I. Younis, Analytical study of the snap-through and bistability of beams with arbitrarily initial shape, J. Mech. Robot. 12 (2020) 041001.
[56] T.J. Rogers, T. Friis, A latent restoring force approach to nonlinear system identification, Mech. Syst. Sig. Process. 180 (2022) 109426, https://doi.org/10.1016/j.ymssp.2022.109426.
[57] R. Ceravolo, Use of instantaneous estimators for the evaluation of structural damping, J. Sound Vib. 274 (2004) 385–401, https://doi.org/10.1016/j.jsv.2003.05.025.
[58] F. Magalhães, Á. Cunha, E. Caetano, R. Brincker, Damping estimation using free decays and ambient vibration tests, Mech. Syst. Sig. Process. 24 (2010) 1274–1290.
[59] F.M. Nogueira, F.S. Barbosa, Novel approach for precise identification of vibration frequencies and damping ratios from free vibration decay time histories data of nonlinear single degree of freedom models, Int. J. Non Linear Mech. 167 (2024) 104867.
[60] Y.-C. Zeng, H. Ding, J.-C. Ji, X.-Y. Mao, L.-Q. Chen, A tristable nonlinear energy sink with time-varying potential barriers, Commun. Nonlinear Sci. Numer. Simul. 142 (2025) 108559.
[61] J.K. Hammond, P.R. White, The analysis of non-stationary signals using time-frequency methods, J. Sound Vib. 190 (1996) 419–447, https://doi.org/10.1006/jsvi.1996.0072.
[62] S. Mallat, G. Papanicolaou, Z. Zhang, Adaptive covariance estimation of locally stationary processes, The Annals of Statistics 26 (1998), https://doi.org/10.1214/aos/1030563977.
[63] J.P. Norenberg, A. Cunha Jr, S. da Silva, P.S. Varoto, Probabilistic maps on bistable vibration energy harvesters, Nonlinear Dyn. 111 (2023) 20821–20840.
[64] L.F. Fadel Miguel, R.H. Lopez, D. Ambrosini, Performance-based optimization of inerter-assisted T-NESs considering SSI effects, Mech. Syst. Signal Proc. 225 (2025) 112277, https://doi.org/10.1016/j.ymssp.2024.112277.
[65] K. Yang, Q. Zhou, Robust optimization of a dual-stage bistable nonlinear vibration energy harvester considering parametric uncertainties, Smart Mater. Struct. 28 (2019) 115018.
[66] A. Lye, L. Marino, A. Cicirello, E. Patelli, Sequential ensemble monte carlo sampler for on-line bayesian inference of time-varying parameter in engineering applications, ASCE-ASME J. Risk Uncert. Eng. Syst. Part B: Mech. Eng. 9 (2023) 031202, https://doi.org/10.1115/1.4056934.
[67] K. Worden, E.J. Cross, A Tutorial on Data-Driven Methods in Nonlinear Dynamics, in: Nonlinear Structures & Systems, 1st ed., River Publishers, New York, 2025, pp. 51–70, https://doi.org/10.1007/978-3-031-36999-5_8.
[68] A.B. Abdessalem, N. Dervilis, D. Wagg, K. Worden, Model selection and parameter estimation in structural dynamics using approximate Bayesian computation, Mech. Syst. Sig. Process. 99 (2018) 306–325.
[69] M. Chiachio, J.L. Beck, J. Chiachio, G. Rus, Approximate Bayesian computation by subset simulation, SIAM J. Sci. Comput. 36 (2014) A1339–A1358.
[70] R. Ceravolo, S. Erlicher, L. Zanotti Fragonara, Comparison of restoring force models for the identification of structures with hysteresis and degradation, J. Sound Vibrat. 332 (2013) 6982–6999, https://doi.org/10.1016/j.jsv.2013.08.019.
[71] G. Abbiati, R. Ceravolo, C. Surace, Time-dependent estimators for on-line monitoring of full-scale structures under ambient excitation, Mech. Syst. Sig. Process. 60–61 (2015) 166–181, https://doi.org/10.1016/j.ymssp.2014.10.018.
[72] L. Cohen, The uncertainty principle in signal analysis, in: Proceedings of IEEE-SP International Symposium on Time-Frequency and Time-Scale Analysis, IEEE, 1994, pp. 182–185.
[73] H.D. Peter, Kernel estimation of a distribution function, Commun. Stat.- Theory Methods 14 (1985) 605–620, https://doi.org/10.1080/03610928508828937.
[74] M. Vorkapić, M. Baltić, B. Fidanovski, M. Vasić, D. Bajić, Thermo-mechanical resistance of additively manufactured carbon fiber-reinforced PLA, Procedia Struct. Integrity 72 (2025) 470–478.
[75] S. Ambati, R. Ambatipudi, Effect of infill density and infill pattern on the mechanical properties of 3D printed PLA parts, Mater. Today: Proc. 64 (2022) 804–807, https://doi.org/10.1016/j.matpr.2022.05.312.

[76] R. Ceravolo, G. Abbiati, Time domain identification of structures: comparative analysis of output-only methods, J. Eng. Mech. 139 (2013) 537–544, https://doi.org/10.1061/(ASCE)EM.1943-7889.0000503.
[77] M. Feldman, Hilbert transform methods for nonparametric identification of nonlinear time varying vibration systems, Mech. Syst. Sig. Process. 47 (2014) 66–77, https://doi.org/10.1016/j.ymssp.2012.09.003.
[78] M. Feldman, Non-linear free vibration identification via the hilbert transform, J. Sound Vib. 208 (1997) 475–489, https://doi.org/10.1006/jsvi.1997.1182.
[79] K. Worden, G.R. Tomlinson, in: Nonlinearity in Structural Dynamics: Detection, Identification and Modelling, 1st ed., CRC Press, 2019 https://doi.org/10.1201/9780429138331.
[80] M. Feldman, Considering high harmonics for identification of non-linear systems by Hilbert transform, Mech. Syst. Sig. Process. 21 (2007) 943–958.
[81] M. Feldman, S. Braun, Nonlinear vibrating system identification via Hilbert decomposition, Mech. Syst. Sig. Process. 84 (2017) 65–96, https://doi.org/10.1016/j.ymssp.2016.03.015.
[82] Z. Wu, S. Seguy, M. Paredes, Qualitative analysis of the response regimes and triggering mechanism of bistable NES, Nonlinear Dyn. 109 (2022) 323–352.
[83] Y. Yang, M.J. Wainwright, M.I. Jordan, On the computational complexity of high-dimensional Bayesian variable selection, (2016).
[84] A. Curtis, A. Lomax, Prior information, sampling distributions, and the curse of dimensionality, Geophysics 66 (2001) 372–378.
[85] A. Salvatore, B. Carboni, W. Lacarbonara, Nonlinear dynamic response of an isolation system with superelastic hysteresis and negative stiffness, Nonlinear Dyn. 107 (2022) 1765–1790.
[86] A. Salvatore, B. Carboni, W. Lacarbonara, Nonlinear dynamic response of an isolation system with negative stiffness and shape memory-based damping. International Design Engineering Technical Conferences and Computers and Information in Engineering Conference, American Society of Mechanical Engineers, 2020.